

## RESEARCH ARTICLE

# Local Trajectory Planning for Obstacle Avoidance of Unmanned Tracked Vehicles Based on Artificial Potential Field Method

LI ZHAI<sup>1</sup>, (Member, IEEE), CHANG LIU<sup>1</sup>, XUEYING ZHANG<sup>2</sup>, AND CHENGPING WANG<sup>3</sup><sup>1</sup>National Engineering Laboratory for Electric Vehicles, Beijing Institute of Technology, Beijing 100081, China<sup>2</sup>China North Vehicle Research Institute, Beijing 100072, China<sup>3</sup>Huawei Technologies Company Ltd., Shanghai 200121, China

Corresponding author: Li Zhai (zhaili26@bit.edu.cn)

This work was supported by the National Key Research and Development Project under Grant 2022YFB2502702.

**ABSTRACT** A trajectory planning method for local obstacle avoidance based on an improved artificial potential field (APF) method is proposed, which is aimed at the problem for dual motor driven unmanned tracked vehicles avoiding dynamic and static obstacles in unstructured environments. Firstly, in traditional artificial potential fields, by adding virtual target points, unmanned tracked vehicles can avoid large obstacles and reach the target point in off-road environments. Secondly, a water droplet type repulsive potential field function for static obstacles and an improved dynamic obstacle potential field function including relative velocity function and relative acceleration function are established in the proposed improved APF method to improve the smoothness of lane changing obstacle avoidance paths. The simulation results of overtaking and obstacle avoidance in the same direction show that the change in heading angle is reduced by 42.9%, and the lateral displacement is reduced by 39.5%. Finally, a trajectory planning method based on improved APF for obstacle avoidance and lane changing of the unmanned tracked vehicle is constructed, which also considers the speed planning with kinematic and dynamic constraints. For obstacle avoidance under lateral meeting condition, the collaborative simulation results of Prescan-Adams-Matlab/Simulink show that the change in heading angle is reduced by 84%, and the lateral displacement is almost zero. Under complex working conditions with multiple static and dynamic obstacles, the results of hardware in loop (HIL) simulation testing and vehicle experiments show that the number of drastic changes in turning radius and heading angle of the vehicle is significantly reduced, and the maximum amplitude was reduced by 63.2% and 37.5% respectively, making the vehicle's obstacle avoidance and lane changing safer, smoother, and more efficient.

**INDEX TERMS** Dual motor driven unmanned tracked vehicles, artificial potential field (APF), obstacle avoidance, trajectory planning.

## I. INTRODUCTION

Tracked vehicles have the advantages of good performance, large bearing capacity, low ground to ground pressure, and zero radius steering, making them the main platforms for transporting military personnel and materials. With the advancement of unmanned, intelligent, and collaborative combat concepts, ground unmanned tracked vehicles have become a hot topic in military equipment research both

domestically and internationally. There is of great significance in reducing casualties, improving combat effectiveness, and building future intelligent transportation and combat systems. Trajectory planning is an important function of intelligent driving for unmanned tracked vehicles, including global planning and local planning. Based on known static obstacles and road information, global planning will plan a path for unmanned tracked vehicles. However, this planning does not take into account the impact of vehicle dimensions and real-time changes in environmental information. Local planning will plan a collision avoidance path from the current

The associate editor coordinating the review of this manuscript and approving it for publication was Shaohua Wan.

location point to a certain sub target point based on real-time road information and dynamic obstacle information obtained by intelligent sensors. In actual off-road driving, not only static obstacles but also various dynamic obstacles will be encountered. Therefore, how to effectively achieve obstacle avoidance local trajectory planning for unmanned tracked vehicles in complex and ever-changing work scenarios has become a major challenge [1].

Autonomous vehicle obstacle avoidance trajectory planning includes two parts: path planning and speed planning. The commonly used local path planning methods usually include the following four categories: parameter curve method, random sampling method, graph search method, method based on optimization, etc. The commonly used parametric curve methods mainly include Bézier curve etc., [2], [3], and [4]. This method generally has good smoothness and real-time performance. Most planning algorithms based on random sampling originate from the field of robotics. Typical algorithms include Probabilistic Roadmap (PRM) and Rapidly-exploring Random Trees (RRT) [5], [6]. These algorithms lack motion constraints and the planned path may not be the optimal path. Common graph search methods include Dijkstra algorithm, A\* algorithm, etc. These methods require searching for target points on a large scale to minimize the global cost of search results, resulting in high computational complexity and low operational efficiency [7], [8]. Planning methods based on optimization, such as swarm intelligence algorithms, can better consider the kinematic and dynamic characteristics of vehicles during planning, but the processing form of obstacle information is relatively single, and the calculation of constraints is also complex and time-consuming [9], [10], [11]. In [12], based on the idea of fuzzy C-means clustering and the ant colony optimization algorithm, the problem of real-time task reallocation of UAV formations in complex and dynamic environments is resolved. Different deep reinforcement learning technologies can be effectively used for different levels of autonomous vehicle motion planning [13], but they rely too much on computing power and have security problems. In recent years, thanks to the explosive evolution of 6G, Artificial intelligence, Blockchain, Cloud computing, Data, and Mobile Edge Computing (MEC) (6G+ABCDE), it is possible to make Intelligent Transportation Systems (ITS) more autonomous, intelligent, and efficient [14], [15].

The artificial potential field (APF) method is widely used in obstacle avoidance trajectory planning for intelligent vehicles due to its simple calculation and good real-time performance [16], [17], [18], [19], [20]. However, the traditional artificial potential field method has the problems of local minima and Goal Nonreachable with Obstacles Nearby (GNRON). In [21], an enhanced attractive potential field function and a repulsive potential field function have been proposed to solve the problem of local minima and GNRON in path planning when encountering static obstacles. But, the situation of dynamic obstacles was not considered. In [22],

an adaptive domain APF method, which dynamically adjusts the field value, is proposed to solve the local minima when avoiding static obstacles, but it will increase the planned path. In [23], the local minima problem was solved by adding virtual target points, ultimately guiding the robot to avoid static obstacles such as traps, but the problem of GNRON was not discussed. In [24], an adjustment factor is added to the repulsive force function to solve the GNRON, but the definition of the adjustment factor is not specifically described. In [25], By introducing a rotating potential field, the UAVs can escape from the common local minimum and oscillations efficiently. The above research on the problem of GNRON in the APF is mainly focused on civilian wheeled vehicles and robots, where the area of obstacles encountered is equivalent to or smaller than that of their own vehicles. However, unmanned tracked vehicles may encounter large obstacles such as hills during off-road driving. The above methods cannot solve the problem of GNRON for large obstacles.

Although local obstacle avoidance path planning for dynamic obstacles can be achieved by improving the potential field function, there are still some problems. In [26], the APF function is improved by establish longitudinal and lateral safety distance models, and it realized path planning for intelligent vehicles to actively avoid static obstacles. In [27], the APF method was applied to vehicle path planning. Specifically, when encountering dynamic obstacles, braking or lane changing is used to avoid them, taking into account the effects of the obstacle's acceleration, deceleration, and mass. In [28], a virtual potential field detection circle model (VPFDCM) with adjustable radius is proposed to achieve effective avoidance of dynamic obstacles. In [29], by defining the safety distance as a variable threshold, such that the forces of the potential field could be adjusted automatically. Based on the dynamic artificial potential field (DAPF) algorithm, this paper provides advisories on how to generate a real-time reactive collision-free path for unmanned aircraft vehicles flying in a dynamic airspace. Zhang et al. conducted obstacle avoidance planning for passing in the same direction by improving the repulsive force adjustment factor and the repulsive force range in [30]. Few factors have been considered in improving the repulsive potential field function, and there has been no discussion on the path planning of lateral dynamic obstacle avoidance in [29] and [30]. In [31], Yadollah et al. integrated APF with optimal control, adding vehicle dynamics constraints. However, this method can reduce the computational efficiency of path planning, and cannot ensure good real-time performance of path planning. The path planning based on APF method in the above studies mostly focuses on the single working condition of robots or intelligent vehicles on urban structured roads. Due to the presence of various obstacles such as dynamic obstacles in the off-road environment, the obstacle avoidance conditions of tracked vehicles are complex and the road conditions are variable. Therefore, the potential field function of dynamic obstacles in APF is constructed in this paper.

Compared with wheeled vehicles, there is relatively little research on trajectory planning for tracked unmanned platforms using APF. In [32], a trajectory tracking controller with feedback correction was designed based on model predictive control method to systematically handle the modeling errors, environmental constraints, and actuator saturations. In [33], The extended Kalman filter (EKF) method and the Levenberg-Marquardt(L-M) method are used to estimate the sliding parameters in the steering process, and the vehicle trajectory prediction is completed. The [34] focused on the trajectory tracking control problem for an articulated unmanned ground vehicle and proposed a rolling prediction range estimation method based on nonlinear model predictive control. A motion planning method based on the offline generation and online extension and selection of motion primitives is proposed for planning the motion of heterogeneous tracked vehicles in [35]. The path planning research mentioned above are not suitable for local obstacle avoidance path planning in scenes with various dynamic and static obstacles. Previously, only path planning research on tracked unmanned platforms was conducted, without considering speed planning at the same time. Therefore, it cannot be guaranteed that unmanned tracked vehicles can safely avoid obstacles during driving.

In order to solve the obstacle avoidance trajectory planning of tracked unmanned platforms in complex scenarios, a local trajectory planning method based on an improved APF method is proposed. The contributions can be summarized as follows:

(1) The GNRON problem caused by large obstacles surrounding the target point has not been solved in the traditional APF method for wheeled vehicles. An improved potential function is proposed to change the direction and magnitude of potential field forces by adding virtual target points, enabling unmanned tracked vehicle to avoid large obstacles and reach the target point in off-road environments.

(2) In response to the problem of large path curvature and long distance in APF planning using circular repulsive potential field functions, a water droplet type repulsive potential field function for static obstacles and an improved dynamic obstacle potential field function including relative velocity function and relative acceleration function are established in the proposed improved APF method, which improves the smoothness of lane changing obstacle avoidance paths.

(3) Under complex working conditions with multiple static and dynamic obstacles, a trajectory planning method for obstacle avoidance and lane changing of the unmanned tracked vehicle is constructed, which also considers the speed planning with kinematic and dynamic constraints.

This paper is organized as follows. The kinematics and dynamics model of a dual electric drive tracked vehicle is established in Section II. An improved APF method for path planning is proposed in Section III, which also includes establishing a collision detection model for obstacle avoidance planning of tracked vehicles. A speed planning method based on complex operating conditions is proposed

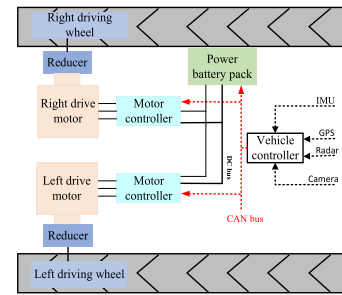


FIGURE 1. Schematic diagram of the double motor driven tracked vehicle system structure.

in Section IV, which implements obstacle avoidance trajectory planning for tracked vehicles. In Section V, the Prescan-Adams-Matlab/Simulink joint simulation and hardware in loop experiments based on dSPACE were conducted. In Section VI, we summarize our contributions and discuss future work.

## II. SYSTEM MODELING AND PROBLEM STATEMENT

### A. SYSTEM STRUCTURE OF A TRACKED VEHICLE DRIVEN BY DUAL MOTORS

The transmission system of a tracked vehicle driven by dual motors mainly consists of two drive motors, two motor controllers, and two reducers, as shown in Figure 1. The transmission system is a multivariable and nonlinear system.

### B. KINEMATICS MODEL OF THE TRACKED VEHICLE DRIVEN BY DUAL MOTORS

The stepless steering of the tracked vehicle driven by dual motors is achieved by controlling the speed difference between the tracks on both sides. The kinematic model of the tracked vehicle in a plane rectangular coordinate system  $XOY$  is shown in the Figure 2. In Figure 2,  $P(x, y)$  denotes the centroid coordinate of the vehicle,  $O$  denotes the instantaneous steering center of the vehicle,  $R$  denotes the steering radius of the vehicle,  $v$  denotes vehicle centroid velocity, and  $\omega$  denotes the angular velocity.

As shown in Figure 2, According to theoretical mechanics, the kinematic model of tracked vehicles can be expressed as follows:

$$\begin{cases} \dot{x} = \frac{1}{2}(v_L + v_R) \cos \theta \\ \dot{y} = \frac{1}{2}(v_L + v_R) \sin \theta \\ \dot{\theta} = \frac{1}{B}(v_L - v_R) \end{cases} \quad (1)$$

where  $v_L$  is the linear speed of the outer track,  $v_R$  is the linear speed of the inner track;  $B$  is the center distance between the two tracks,  $L$  is the grounding length between the track and the ground, and  $\theta$  is the heading angle.

### C. STEERING DYNAMICS MODEL OF THE TRACKED VEHICLE DRIVEN BY DUAL MOTORS

As shown in Figure 3, there are many steering conditions for the tracked vehicle driven by dual motors. In the Figure 3,

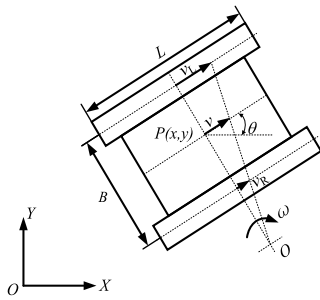


FIGURE 2. Steering kinematics analysis of the tracked vehicle.

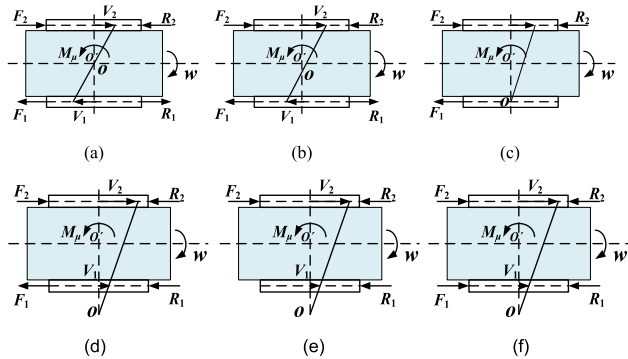


FIGURE 3. Force analysis under (a) center steering, (b)  $0 < R < 0.5B$ , (c)  $R = 0.5B$ , (d) Brake steering, (e) Free steering, (f) Driving steering.

$F_1$  and  $F_2$  denote the traction forces of the inner motor and outer motor respectively,  $F_{f1}$  and  $F_{f2}$  denote the longitudinal friction resistances of the tracks on both sides when steering,  $v_1$  and  $v_2$  denote the speeds of the tracks,  $M_\mu$  is the steering resistance torque,  $\omega$  is the steering angular speed,  $R_0$  is the free steering radius.

1) SMALL RADIUS STEERING CONDITION ( $R < 0.5B$ )

The small radius steering conditions mainly include three working conditions, namely  $R = 0$ ,  $0 < R < 0.5B$  and  $R = 0.5B$ , as shown in Figure 3(a), (b) and (c) respectively.

Taking the case of  $0 < R < 0.5B$  as an example, the relationship between the forces and the moment of the tracked vehicle during small radius steering is expressed as follows:

$$\begin{cases} F_1 - F_2 + F_{f2} - F_{f1} = m\dot{v}_y \\ (F_1 + F_2) \cdot \frac{B}{2} - (F_{f1} + F_{f2}) \cdot \frac{B}{2} - M_\mu = J\dot{\omega} \end{cases} \quad (2)$$

where  $m$  the vehicle mass,  $v_y$  is the longitudinal speed,  $F_1$  and  $F_2$  are the driving forces in opposite directions,  $v_1$  is greater than  $v_2$  and they have opposite directions.

2) LARGE RADIUS STEERING CONDITION ( $R > 0.5B$ )

The large radius steering conditions mainly include three conditions, namely  $0.5B < R < R_0$ ,  $R = R_0$  and  $R > R_0$ , as shown in Figure 3(d), (e) and (f) respectively.  $R_0$  is the free steering radius of the tracked vehicle.

Taking the brake steering in Figure 3(b) as an example, the relationship between the forces and the moment of tracked

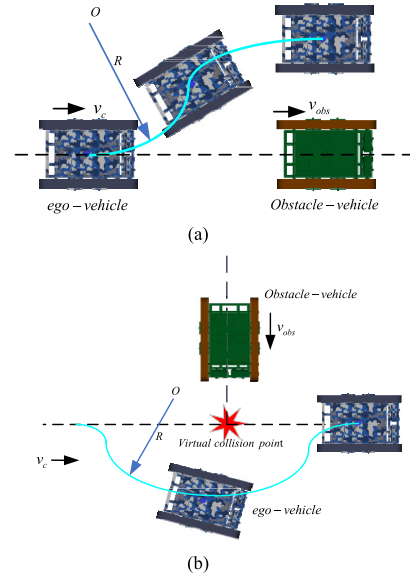


FIGURE 4. Schematic diagram of the obstacle avoidance scene. (a) Obstacle avoidance under overtaking in the same direction (b) Obstacle avoidance under transverse meeting.

vehicles is expressed as follows:

$$\begin{cases} F_1 - F_2 - F_{f1} - F_{f2} = m\dot{v}_y \\ (F_1 + F_2) \cdot \frac{B}{2} + (F_{f2} - F_{f1}) \cdot \frac{B}{2} - M_\mu = J\dot{\omega} \end{cases} \quad (3)$$

where  $F_1$  is the driving force of the outer track;  $F_2$  is the braking force of the inner track, which is opposite to the speed direction of the inner track.

$F_{f1}$  and  $F_{f2}$  can be defined as follows:

$$F_{f1,2} = \frac{\mu mg}{2} \quad (4)$$

$M_z$  can be defined as follows:

$$M_z = \frac{\mu mgL}{4} \left[ 1 + \left( \frac{2d}{L} \right)^2 \right] \quad (5)$$

According to the force analysis of the tracked vehicle, the output torque  $T_{1,2}$  and output power  $P_{1,2}$  of the motors on both sides are expressed as follows:

$$\begin{cases} T_{1,2} = \frac{F_{1,2}}{i\eta} \cdot r \\ P_{1,2} = \frac{T_{1,2} \cdot n_{1,2}}{9549} \end{cases} \quad (6)$$

After the stress analysis of tracked vehicles is completed, based on the d'Alembert principle, the dynamic equation of tracked vehicles is established as follows:

$$\begin{bmatrix} m & 0 & 0 \\ 0 & m & 0 \\ 0 & 0 & J \end{bmatrix} \begin{bmatrix} \ddot{x} \\ \ddot{y} \\ \ddot{\theta} \end{bmatrix} = \frac{1}{r} \begin{bmatrix} \cos \theta & \cos \theta \\ \sin \theta & \sin \theta \\ B/2 & -B/2 \end{bmatrix} \begin{bmatrix} T_1 \\ T_2 \end{bmatrix} + \begin{bmatrix} \sin \theta \\ -\cos \theta \\ 0 \end{bmatrix} \lambda \quad (7)$$

where,  $\theta$  is the angle between the vehicle and the x-axis,  $\lambda$  is constraint vector, expressed as:  $\lambda = -m\dot{\theta} (\dot{x} \cos \theta + \dot{y} \sin \theta)$ .

### D. OBSTACLE AVOIDANCE MODEL OF TRACKED VEHICLES

In order to ensure safe trajectory planning, current and future movements of the obstacle vehicles should be considered. The obstacles considered in this paper are tracked vehicles, and the time step of the planning problem is  $\Delta t$ .

Assuming that the heading angle, the velocity and the angular velocity of the obstacle vehicle can be measured, in order to effectively predict the future state of the obstacle vehicle, the obstacle vehicle model is described using a discrete equation system and represented as follows:

$$\begin{cases} x_{obs}(t + \Delta t) = x_{obs}(t) + \frac{1}{2}(v_L + v_R) \cos \theta \cdot \Delta t \\ y_{obs}(t + \Delta t) = y_{obs}(t) + \frac{1}{2}(v_L + v_R) \sin \theta \cdot \Delta t \\ \theta_{obs}(t + \Delta t) = \theta_{obs}(t) + \frac{1}{B}(v_L - v_R) \cdot \Delta t \end{cases} \quad (8)$$

The two obstacle avoidance scenarios of the overtaking in the same direction and crossing in the transverse direction are studied in this paper, as shown in Figure 4. The prerequisite for the lane changing scenarios for obstacle avoidance shown in Figure 4 (a) is:  $v_{obs} < v_c$ . The minimum longitudinal distance  $D_c$  required for the lane changing at this time can be expressed as:

$$D_c = 2 \frac{v_c - v_{obs}}{v_c} \sqrt{R^2 - \left(R - \frac{L}{2}\right)^2} \quad (9)$$

where,  $L$  is the width of the transverse lane change.

## III. LOCAL OBSTACLE AVOIDANCE PATH PLANNING ALGORITHM BASED ON THE IMPROVED APF

### A. TRADITIONAL APF

#### 1) FUNCTIONS OF THE ATTRACTIVE POTENTIAL FIELD AND THE REPULSIVE POTENTIAL FIELD

The attractive potential field function  $U_{att}$  and the repulsive potential field function  $U_{rep}$  are respectively represented as follows

$$U_{att} = \frac{1}{2} k_{att} d_{goal}^2 \quad (10)$$

$$U_{rep} = \begin{cases} \frac{1}{2} k_{rep} \left(\frac{1}{d_{obs}} - \frac{1}{d_0}\right)^2 d_{obs} \leq d_0 \\ 0 \quad d_{obs} > d_0 \end{cases} \quad (11)$$

where,  $(x, y)$  denotes the position coordinate of the vehicle in a two-dimensional coordinate system,  $(x_g, y_g)$  is the target point coordinate of the moving vehicle,  $(x_{obs}, y_{obs})$  is the position coordinate of the obstacle vehicles,  $k_{att}$  and  $k_{rep}$  represent the proportional coefficients of the attractive and repulsive potential fields, respectively.  $d_0$  is the maximum distance that an obstacle can exert repulsive force on the vehicle.  $d_{goal}$  and  $d_{obs}$  represent the distance between the ego-vehicle and the target point or the obstacles, respectively. By solving the negative gradients of the attractive potential field function  $U_{att}$  and the repulsive force potential field function  $U_{rep}$  respectively. The attractive function  $F_{att}$  and the repulsive force function  $F_{rep}$  are obtained as follows:

$$F_{att} = -\nabla U_{att} = -k_{att} d_{goal} \quad (12)$$

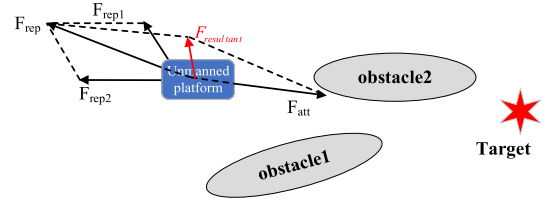


FIGURE 5. The problem of GNRN caused by multiple large obstacles surrounding the target point.

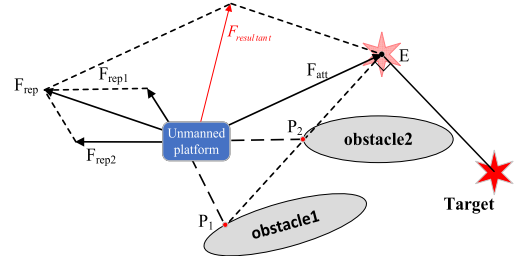


FIGURE 6. Schematic diagram of adding a virtual target points.

$$F_{rep} = -\nabla U_{rep} = \begin{cases} k_{rep} \left(\frac{1}{d_{obs}} - \frac{1}{d_0}\right) \frac{\nabla d_{obs}}{d_{obs}^2} d_{obs} \leq d_0 \\ 0 \quad d_{obs} > d_0 \end{cases} \quad (13)$$

#### 2) RESULTANT POTENTIAL FIELD FUNCTION

The ego-vehicle moves under the combined potential field composed of the target point and multiple obstacles. According to the attractive potential field function of the target point and the repulsive potential field function of the obstacles, and superposing the potential fields, the combined potential field function  $U$  can be obtained as follows:

$$U = U_{att} + \sum_{i=1}^n U_{rep} \quad (14)$$

The resultant force  $F$  acting on the vehicle is obtained by adding  $F_{att}$  and  $F_{rep}$ , and its expression is as follows:

$$F = -\nabla U = F_{att} + \sum_{i=1}^n F_{rep} \quad (15)$$

where  $n$  is the number of obstacles that generate repulsive force on the ego-vehicle.

### B. IMPROVED APF

#### 1) IMPROVEMENT OF LOCAL MINIMUM AND GNRN

To solve the problem of local minimum, in [36], the ego-vehicle can escape from the local minimum trap by setting a virtual target point and changing the gravity and repulsion forces, and a simulation model is established to verify the effectiveness and reliability of the algorithm.

As the vehicle gradually moves towards the target point, the direction of the resultant force acting on the vehicle will constantly change. When the target point is obstructed by irregular large obstacles in Figure 5, there will be a situation where the combined force is equal to 0, which can lead to

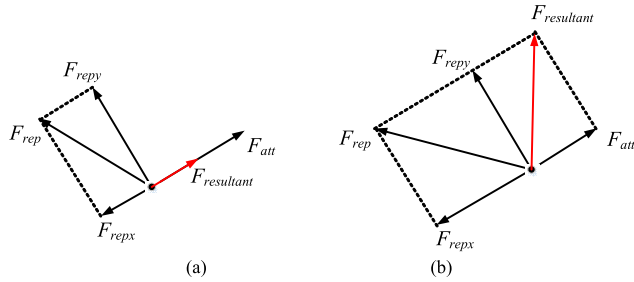


**FIGURE 7. Schematic diagram of decomposed repulsion force**  
 (a)  $|F_{repx}| < |F_{att}|$  (b)  $|F_{repx}| \geq |F_{att}|$ .

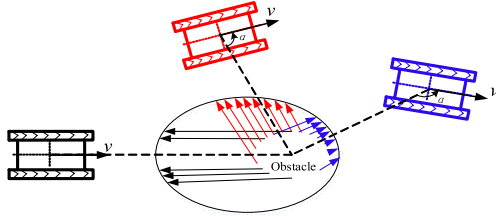


**FIGURE 8. Schematic diagram of the relationship between the repulsion force of the obstacle and the position of vehicle.**

the problem of Goal Nonreachable with Obstacles Nearby (GNRON).

To solve GNRON, based on the boundaries of the irregular large obstacles and the orientation of the actual target point, a virtual target point is constructed to ultimately guide the vehicle to reach the actual target point, as shown in Figure 6. The points  $P_1$  and  $P_2$  closest to the current position of the vehicle on the obstacle boundary are selected, as shown in the Figure 6. Firstly, the  $P_1$  and  $P_2$  points are connected, and then a straight line perpendicular to the extension line of the line  $P_1P_2$  is drawn through the center of the target point, intersecting with the line  $P_1P_2$  at point  $E$ . Finally, a virtual target point is obtained centered around point  $E$ . From Figure 6,  $F_{resultant}$  is the new resultant force of the vehicle.

$$F_{resultant} = F_{att} + F_{rep} \quad (16)$$

$$F_{rep} = F_{rep1} + F_{rep2} \quad (17)$$

In order to solve the problem of GNRON and enable the vehicle to reach the target point as soon as possible, as shown in Figure 7, the repulsive force  $F_{rep}$  of obstacle in the potential field are decomposed along the gravitational direction and perpendicular to the gravitational direction, and the decomposed repulsive forces are recorded as  $F_{repx}$  and  $F_{repy}$ , respectively. The calculation of the resultant force is specified as two cases in Figure 7:

Comparing  $F_{repx}$  and  $F_{att}$ , if  $|F_{repx}| < |F_{att}|$ , then let  $F_{repy} = 0$ , and the resultant force of the potential field on the vehicle is expressed as follows:

$$F_{resultant} = F_{att} + F_{repx} \quad (18)$$

If  $|F_{repx}| \geq |F_{att}|$ , then let  $F_{repx} = 0$ , and the resultant force of the potential field on the vehicle is:

$$F_{resultant} = F_{att} + F_{repy} \quad (19)$$

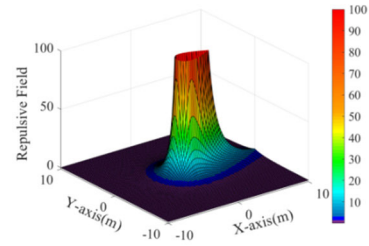


**FIGURE 9. Improved repulsive potential field of a water droplet type.**

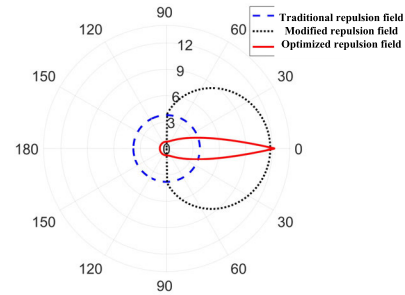


**FIGURE 10. Comparison and analysis of obstacle repulsion field.**

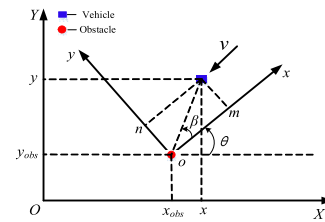


**FIGURE 11. Schematic diagram of the coordinate conversion.**

## 2) IMPROVEMENT OF DYNAMIC PLANNING EFFECT

### (1) Improvement of the repulsion potential field of the static obstacle

In the traditional APF, the repulsive potential field is related to the distance from the obstacle to the vehicle, and the potential field force values are uniformly distributed around the position of the obstacle, as shown in Figure 8.  $\alpha$  represents the angle between the velocity  $v$  and the position line connecting ego-vehicle and obstacle. As the vehicle moves towards the obstacle,  $\alpha$  gradually increases, and the repulsive force generated by the obstacle should increase as the distance between ego-vehicle and obstacle decreases.

A distance adjustment factor  $k_d$  related to  $\alpha$  is added in the improved repulsive potential field function, which is expressed as follows:

$$U_{rep} = \begin{cases} \frac{1}{2} k_{rep} (\frac{1}{k_d \cdot d_{obs}} - \frac{1}{d_0})^2 d_{obs} \leq d_0 \\ 0 & d_{obs} > d_0 \end{cases} \quad (20)$$

$$k_d = \begin{cases} \sin \alpha + m_d \alpha \in (0, \pi/2) \\ 1 + m_d & \text{Others} \end{cases} \quad (21)$$

where  $m_d$  is a constant and set to 0.6.

Taking the derivative of the Eq.(20), the repulsive force of the static obstacle  $F_{rep}$  is expressed as follows:

$$F_{rep} = \begin{cases} \frac{k_{rep}}{k_d^2} \left( \frac{1}{k_d \cdot d_{obs}} - \frac{1}{d_0} \right) \frac{1}{d_{obs}^2} d_{obs} \leq d_0 \\ 0 \quad d_{obs} > d_0 \end{cases} \quad (22)$$

According to Eq.(22), the three-dimensional representation of  $F_{rep}$  is shown in Figure 9, presenting the shape of a water droplet. This means that  $F_{rep}$  gradually decreases with increasing distance between ego-vehicle and obstacle.

As shown in Figure 10, a comparison of the improved obstacle repulsion field proposed in this article with the traditional APF and the APF proposed by other researchers has been made. The numerical values in Figure 10 represents the angle  $\alpha$ , with a range of 0-180°. It can be seen that the repulsive field of the traditional APF is a uniform circle, and the repulsive force remains unchanged no matter how the angle  $\alpha$  changes. The repulsion field proposed by other researchers directly becomes 0 when it is greater than 90°, which is also not in line with the actual situation.

## (2) Improvement of the repulsion potential field of the dynamic obstacle

On the basis of the improved repulsion potential field function of the static obstacle, the repulsion potential field function of the dynamic obstacle is reestablished by adding the relative velocity and the relative acceleration.

In order to facilitate the analysis of the relationship between relative velocity, relative acceleration, and relative position, the original coordinate system  $XOY$  is transformed into  $xoy$ . The coordinate transformation relationship is shown in Figure 11. According to the principles of translation and rotation in mathematics, the relationship between the new position coordinate  $(m, n)$  of the vehicle and the old coordinate  $(x, y)$  is expressed as follows:

$$\begin{bmatrix} m \\ n \end{bmatrix} = \begin{bmatrix} \cos \theta & -\sin \theta \\ \sin \theta & \cos \theta \end{bmatrix} \begin{bmatrix} x \\ y \end{bmatrix} - \begin{bmatrix} x_{obs} \cos \theta + y_{obs} \sin \theta \\ -x_{obs} \sin \theta + y_{obs} \cos \theta \end{bmatrix} \quad (23)$$

where,  $\theta$  is the angle between the relative velocity direction and the x-axis direction in  $XOY$ ,  $\beta$  is the angle between the relative velocity and the relative position of the dynamic obstacle and ego-vehicle. It can be obtained as follows:

$$\cos \beta = \frac{m}{\sqrt{m^2 + n^2}} \quad (24)$$

The relative position potential field function  $U_{rep-d}$ , relative velocity potential field function  $U_{rep-v}$  and relative acceleration potential field function  $U_{rep-a}$  are as follows:

$$U_{rep-d} = \begin{cases} \frac{1}{2} k_{rep} \left( \frac{1}{k_d \cdot d_{obs}} - \frac{1}{d_0} \right)^2 & d_{obs} \leq d_0 \\ 0 & d_{obs} > d_0 \end{cases} \quad (25a)$$

$$U_{rep-v} = k_v v_{eo}^2 \cos \beta, \quad \beta \in \left( -\frac{\pi}{2}, \frac{\pi}{2} \right) \quad (25b)$$

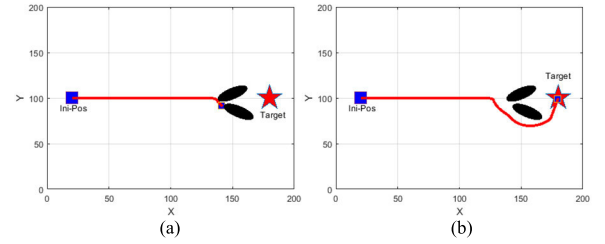


FIGURE 12. Simulation Results of the GNRON solution. (a) Traditional APF (b) Improved APF.

$$U_{rep-a} = k_a a_{eo}^2 \cos \gamma, \quad \gamma \in \left( -\frac{\pi}{2}, \frac{\pi}{2} \right) \quad (25c)$$

where,  $v_{eo}$  is the relative velocity of the dynamic obstacle and ego-vehicle, and  $k_v$  is the proportional coefficient of the relative velocity,  $a_{eo}$  is the relative acceleration,  $k_a$  is the relative acceleration coefficient.

The repulsive potential field function  $U_{rep}$  of the dynamic obstacle is represented as follows:

$$U_{rep} = \begin{cases} \frac{1}{2} k_{rep} \left( \frac{1}{k_d \cdot d_{obs}} - \frac{1}{d_0} \right)^2 + k_v v_{eo}^2 \cos \beta + k_a a_{eo}^2 \cos \gamma, \\ \dots \dots d_{obs} \leq d_0 \text{ and } \beta \in \left( -\frac{\pi}{2}, \frac{\pi}{2} \right) \\ \frac{1}{2} k_{rep} \left( \frac{1}{k_d \cdot d_{obs}} - \frac{1}{d_0} \right)^2, d_{obs} \leq d_0 \text{ and } \beta \\ \notin \left( -\frac{\pi}{2}, \frac{\pi}{2} \right) \\ 0 \quad d_{obs} > d_0 \end{cases} \quad (26)$$

Taking the derivative of Eq. (25a), the repulsive force  $F_{rep-d}$  is obtained as follows:

$$F_{rep-d} = \begin{cases} \frac{k_{rep}}{k_d^2} \left( \frac{1}{k_d \cdot d_{obs}} - \frac{1}{d_0} \right) \frac{1}{d_{obs}^2} d_{obs} \leq d_0 \\ 0 \quad d_{obs} > d_0 \end{cases} \quad (27)$$

By taking the derivative of the position  $d$  in Eq. (25b), the relative velocity repulsion  $F_{rep-v1}$  is obtained as follows:

$$F_{rep-v1} = -\nabla_d U_{rep-v} = -k_v v_{eo}^2 \cdot \frac{\sin \beta}{d_{obs}} (\sin \beta, -\cos \beta) \quad (28a)$$

By taking the derivative of the velocity  $v$  in Eq. (25b), the relative velocity repulsion  $F_{rep-v2}$  is obtained as follows:

$$\begin{aligned} F_{rep-v2} &= -\nabla_v U_{rep-v} = -\nabla_v \left( k_v v_{eo}^2 \cos \beta \right) \\ &= -2k_v v_{eo} \cos \beta \end{aligned} \quad (28b)$$

By deriving of the position and the acceleration for the Eq.(25c) respectively, the relative acceleration repulsion is obtained as follows:

$$F_{rep-a1} = -\nabla_d U_{rep-a} = -k_a a_{eo}^2 \cdot \frac{\sin \gamma}{d_{obs}} (\sin \gamma, -\cos \gamma) \quad (29a)$$

$$F_{rep-a2} = -\nabla_a U_{rep-a} = -2k_a a_{eo} \cos \gamma \quad (29b)$$

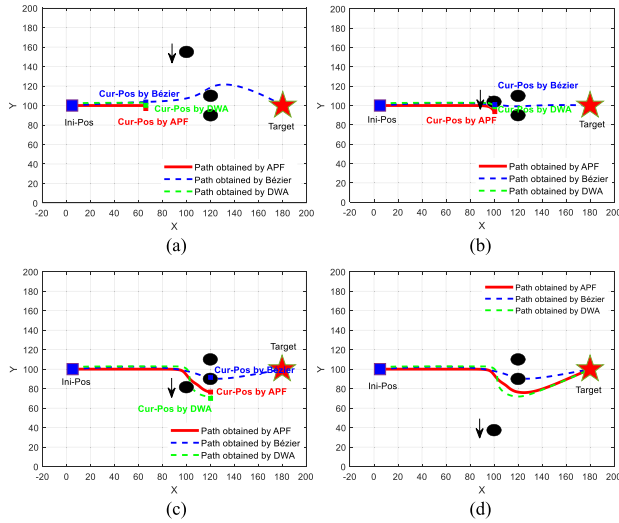


**FIGURE 13.** Comparison of the path planning planned by improved APF, Bézier curve and DWA. (a) Time 1 (b) Time 2 (c) Time 3 (d) Time 4.

where  $\gamma$  denotes the angle between the relative acceleration and the relative position of the dynamic obstacle and ego-vehicle.

Finally, the repulsive force of the dynamic obstacle is obtained as follows:

$$F_{rep} = \begin{cases} F_{rep-d} + F_{rep-v1} + F_{rep-v2} + F_{rep-a1} + F_{rep-a2}, & \dots \dots d_{obs} \leq d_0 \text{ and } \beta \in \left(-\frac{\pi}{2}, \frac{\pi}{2}\right) \\ F_{rep-d} d_{obs} \leq d_0 \text{ and } \beta \notin \left(-\frac{\pi}{2}, \frac{\pi}{2}\right) \\ 0 & d_{obs} > d_0 \end{cases} \quad (30)$$

**(3) Simulation Verification of the algorithm**

(a) Goal Nonreachable with Obstacles Nearby (GNRON) problem

A typical GNRON condition in MATLAB simulation software is established, and the simulation results are shown in Figure 12. As shown in Figure 12(a), when using traditional APF, the vehicle will stop at a certain point and cannot move forward. As shown in Figure 12(b), the vehicle using the improved APF can bypass irregular obstacles and reach the target point in a timely manner.

(b) Complex dynamic obstacle environment

Under complex working conditions with dynamic and static obstacles, the improved APF method, Bézier curve method, and dynamic window method were used to plan the obstacle avoidance trajectory, respectively. In the simulation environment, there are two static obstacles located on one side of the target point, and a dynamic obstacle moves laterally in the negative y-axis direction at a speed of 5m/s, and the initial speed of the ego-vehicle is 10m/s. The simulation results are shown in Figure 13. At time 2, as shown in Figure 13(b), the path planned by the Bézier curve overlaps with the dynamic obstacle, indicating a collision. The curvature of the path planned by DWA suddenly increases, and the path is too close

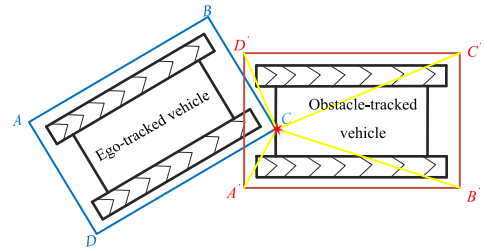


**FIGURE 14.** Schematic diagram of the rectangular collision detection method.

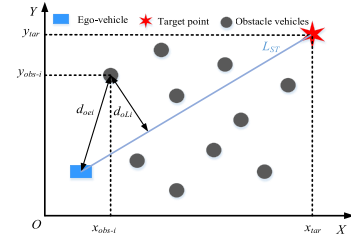


**FIGURE 15.** Schematic diagram of the target inaccessible solution.

to dynamic obstacles. At time 3, as shown in Figure 13 (c), there is a collision point between the path planned by the Bézier curve and the static obstacle. The distance between the path planned by DWA and static obstacles is too large, which reduces planning efficiency. Until time 4, as shown in Figure 13 (d), the obstacle avoidance path planned through the improved APF method is safer, more comfortable, and more efficient. If the obstacle has a high speed, collisions will occur using only the APF method. Therefore, in Section IV, the speed planning method was proposed and incorporated into the APF method to avoid collisions at high speeds of the obstacle.

**IV. SPEED PLANNING OF LOCAL OBSTACLE AVOIDANCE BASED ON WORKING CONDITIONS**

**A. ENVIRONMENTAL INFORMATION PREPROCESSING**

1) OBSTACLE AVOIDANCE DETECTION METHOD FOR TRACKED VEHICLES

A rectangular collision detection method based on the shape of the tracked vehicle and the shape of the dynamic obstacles (generally dynamic vehicles). Its schematic diagram is shown in Figure 14.

To judge whether they will collide, it is only necessary to judge whether point C is inside the rectangle A'B'C'D'.

The judgment equation is as follows:

$$\begin{aligned} & (\vec{A'B'} \times \vec{A'C}) * (\vec{C'D'} \times \vec{C'C}) \geq 0 \& (\vec{B'C'} \times \vec{B'C}) \\ & * (\vec{D'A'} \times \vec{D'C}) \geq 0 \end{aligned} \quad (31)$$

As long as the following expression is met, then point C is located in rectangle A'B'C'D', and the tracked vehicle will collide with the obstacle. Other vertices of rectangle ABCD are also judged by cross product.

2) STATIC OBSTACLE SCREENING MODEL

In Figure 15, first, a virtual straight line L<sub>ST</sub> from current position of tracked vehicle to target position is created. Its

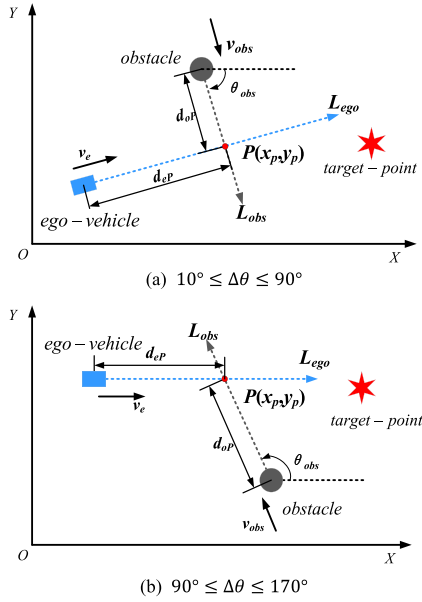


**FIGURE 16.** Schematic diagram of the dynamic planning for lateral meeting. (a)  $10^\circ \leq \Delta\theta \leq 90^\circ$  (b)  $90^\circ \leq \Delta\theta \leq 170^\circ$ .

mathematical expression is as follows:  $L_{ST} : y = k_{ST}x + b_{ST}, x \in (x_{ego}, x_{tar})$

The location coordinate of the  $i - th$  static obstacle in environment is  $(x_{obs-i}, y_{obs-i})$ , and the expressions of  $d_{oei}$  and  $d_{oLi}$  can be obtained as follows:

$$\begin{cases} d_{oei} = \sqrt{(x_{obs-i} - x_{ego})^2 + (y_{obs-i} - y_{ego})^2} \\ d_{oLi} = \frac{|k_{ST} \cdot x_{obs-i} - y_{obs-i} + b_{ST}|}{\sqrt{k_{ST}^2 + 1}} \end{cases} \quad (32)$$

where  $d_{oe}^*$  denotes the collision safety threshold value from static obstacle to tracked vehicle  $d_{oe}^*$ ,  $d_{oL}^*$  denote the collision safety threshold value from static obstacle to straight line  $L_{ST}$  as. When  $d_{oei} < d_{oe}^*$  and  $d_{oLi} < d_{oL}^*$ , it is determined that the corresponding obstacles will affect the subsequent path planning of the ego-vehicle, and screening is required. A large number of obstacle avoidance simulation experiments based on the improved APF algorithm have proven that ego-vehicle can plan efficient and safe obstacle avoidance path when  $d_{oe}^*$  and  $d_{oL}^*$  are taken as 60m and 5m respectively.

### 3) DYNAMIC OBSTACLE SCREENING MODEL

The speed of dynamic obstacle is defined as  $v_{obs}$ , the speed of ego-vehicle is defined as  $v_{ego}$ , and the angle between the two speeds is defined as  $\Delta\theta$ . The definitions of collision safety thresholds  $d'_{oe}$  and  $d'_{oL}$  are as follows:

$$\begin{cases} \cos \Delta\theta = \frac{v_{ego} \cdot v_{obs}}{|v_{ego}| |v_{obs}|} \\ d'_{oe} = (1 + \frac{|v_{ego} - v_{obs}|}{|v_{ego}|}) d_{oe}^* \\ d'_{oL} = (1 + |v_{obs} \cdot \cos \Delta\theta|) d_{oL}^* \end{cases} \quad (33)$$

When both  $d_{oei}$  and  $d_{oLi}$  are below their respective safety thresholds, preliminary screening of dynamic obstacles is

conducted. Furthermore, based on the state information of the remaining dynamic obstacles and ego-vehicles, more precise driving conditions are divided for the next step of local obstacle avoidance trajectory planning.

## B. OBSTACLE AVOIDANCE DECISION BASED ON WORKING CONDITIONS

### 1) OVERTAKING CONDITION IN THE SAME DIRECTION

In the same direction overtaking condition studied in this article, the lateral distance between the obstacle vehicle and the ego-vehicle meets the following requirements:  $d_{oLi} < 3.5m$ . The heading angle of the two is roughly the same, and the speed of the obstacle is lower than the target speed of the ego-vehicle. The remaining working conditions are determined as follows:

$$\begin{cases} \theta_i \in (-30, 30) \\ (\psi_{ego} - \psi_i) \in (-5, 5) \\ v_i \leq v_{ego} \\ D_{ego-i} \leq 2 + W_i/2 \end{cases} \quad (34)$$

where,  $i$  is the ID number of the obstacle identified by the on-board sensor,  $\theta_i$  is the azimuth of the obstacle vehicle and ego-vehicle,  $\psi_{ego}$  and  $\psi_i$  are respectively the heading angle of the ego-vehicle and the obstacle vehicle,  $v_i$  is the speed of the obstacle vehicle,  $v_{ego}$  is the speed of the ego-vehicle,  $D_{ego-i}$  is the distance from the obstacle vehicle to the straight line of the self vehicle axis, and  $W_i$  is the width of the obstacle vehicle. When the azimuth angle, heading angle, speed and lateral distance between the obstacle vehicle and the self vehicle meet the (34), it is considered that the vehicle needs to pass and avoid obstacles at present.

### 2) LATERAL MEETING CONDITION

In the lateral vehicle operating condition, it meets the following requirements:  $10^\circ \leq \Delta\theta \leq 170^\circ$ . As shown in the Figure16, there are mainly two cases: (a)  $10^\circ \leq \Delta\theta \leq 90^\circ$  and (b)  $90^\circ \leq \Delta\theta \leq 170^\circ$ . At this time, it is necessary to first determine whether there is a virtual collision point  $P$  between the ego-vehicle and the obstacle vehicle in their respective driving directions. Secondly, it should be determined whether the time to reach the point  $P$  when the two vehicles are driving at the current speed is within the dangerous time range, which is affected by the speed of the two vehicles. The driving behavior at the next moment should be determined based on the arrival time of the two vehicles at point  $P$  and the driving aggressiveness of each vehicle.

### 3) DEFINITION OF DECISION PRIORITY

The vehicle has been assigned eight driving behaviors, and the priority order of vehicle driving behaviors is defined based on the importance and urgency of different working conditions, as shown in Table 1. When the decision priority is the same, the driving behavior is determined according to the position, the speed and the acceleration information of the vehicles and the obstacles.

TABLE 1. Driving behavior decision priorities.

Driving behavior	Priority
Lateral meeting condition - emergency braking	1
Normal driving condition - emergency braking	1
Lateral meeting condition - slow down	2
Lateral meeting condition - accelerate	2
Lateral meeting condition - constant speed	2
Overtaking condition - accelerate	3
Normal driving condition - constant speed	4
Overtaking condition - constant speed	4

C. SPEED PLANNING OF OBSTACLE AVOIDANCE

1) ACCELERATION AND VELOCITY CONSTRAINTS

(1) Mechanical characteristics limitation of the drive motor

When the required torque of the motor reaches or approaches the peak torque at the current speed, and the steering ability of the vehicle at the current speed will be restricted, which is difficult to meet the performance requirements of speed planning and trajectory tracking control for vehicle.

$\eta$  is the mechanical transmission efficiency,  $i$  is the comprehensive transmission ratio, and  $r$  is the radius of the driving wheel. The selection of road adhesion coefficient  $\mu$  reflects the interaction with the soil ground, and the steering resistance coefficient is expressed using an empirical equation as  $\mu_x = \frac{\mu_{max}}{0.925+0.15\rho}$ ,  $\rho$  is the relative steering radius,  $\rho = R/B$ . The acceleration can be expressed as follows:

$$a = -\min\left(\frac{T_{max}\eta i}{rm}, \frac{\mu_x F_z}{m}\right) \quad (35)$$

When the motor outputs the braking torque, the minimum deceleration of the vehicle equals to  $a$ . When the motor outputs the driving torque, the maximum acceleration of the vehicle  $a_{max}$  equals to  $a$ .

(2) Lateral stability constraints

Regardless of the sideslip angle of the center of mass, the yaw rate is an active control parameter required by the stability control system. The yaw rate increases with the increase of vehicle speed, and starts to decrease when the adhesion limit is reached. From the Eq. (2)-(5) in the section II, it can be seen that the road adhesion coefficient  $\mu$  affects the frictional resistances  $F_{f1}$   $F_{f2}$  and yaw moment  $M_z$ . The yaw rate is constrained by setting  $\mu \in [\mu_{min}, \mu_{max}]$ . The constraint conditions for yaw rate  $\omega$  are as follows:

$$-\frac{\mu g}{v} - \vartheta_\omega \leq \omega \leq \frac{\mu g}{v} + \vartheta_\omega \quad (36)$$

where,  $\vartheta_\omega$  is the relaxation parameter of the yaw rate constraint, which can be adjusted according to the actual control effect required.

Considering the above constraints, the maximum vehicle speed  $v'_{max-slip}$  is obtained and equals to  $\omega R$  according to the actual yaw rate  $\omega$ .

In order to ensure the lateral stability of the vehicle, a safety factor  $\tau = 1.2$  is introduced, and the maximum speed  $v_{max-slip}(t)$  is corrected to  $v'_{max}/\tau$ .

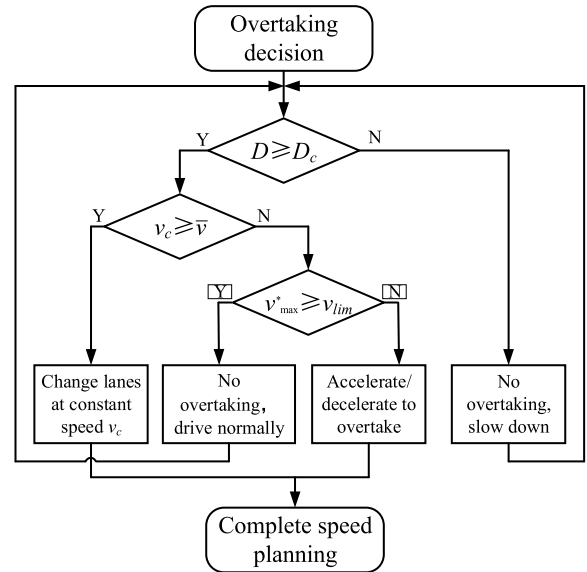


FIGURE 17. Flow chart of the speed planning for obstacle avoidance under overtaking condition.

The constraints on vehicle speed such as pitching, rolling and riding comfort are not considered. So, the boundary conditions for vehicle speed and acceleration constraints in the planning time domain  $T$  are expressed as follows:

$$\begin{cases} v_{max}(t) = \min(v_{max}, v_{max-slip}(t), (v + T \cdot a_{max}(t))) \\ v_{min}(t) = \max(0, (v + T \cdot a_{min}(t))) \\ a_{max}(t) \\ a_{min} \end{cases} \quad (37)$$

2) SPEED PLANNING FOR OVERTAKING AND LATERAL CROSSING OBSTACLE AVOIDANCE

The driving speed is planned based on the following 5 driving behaviors.

(1) Starting acceleration

The speed planning during the starting stage of the vehicle is closely related to the expected speed, and the speed planning function is expressed as follows:

$$\begin{cases} v(t) = a_s \cdot t, n < n_{max}(a_s) \\ v(t) = 0.377n_{max}(a_s)r + \int a(t)dt, n \geq n_{max}(a_s) \end{cases} \quad (38)$$

where  $a_s$  is the given starting acceleration,  $a(t)$  is the real-time acceleration when the backup power is gradually reduced,  $n_{max}(a_s)$  is the maximum speed that the motor can reach when the vehicle accelerates with  $a_s$ , which can be obtained by looking up the table.

(2) Constant speed driving

When the vehicle maintains a constant speed within the planned time domain, the speed of the vehicle can be expressed as:  $v(t) = v$ .

(3) Overtaking

When the front vehicle affects the normal driving of the ego-vehicle, an overtaking at acceleration or a constant

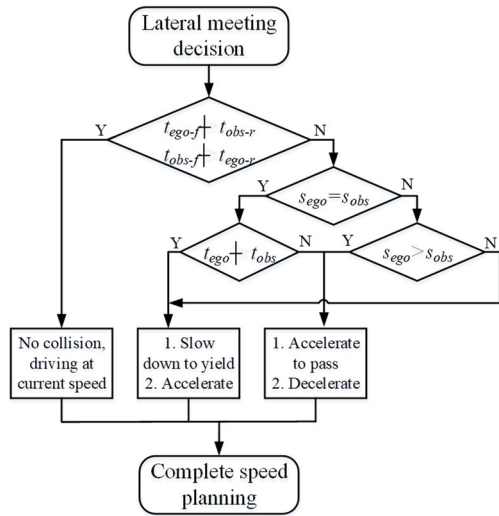


**FIGURE 18.** Flow chart of the speed planning for obstacle avoidance under lateral meeting condition.

speed is required. The speed planning schematic is proposed, as shown in Figure 17.

The meanings of the characters in the Figure 17 are:  $D$  is the distance between the ego-vehicle and the obstacle vehicle in front of it.  $D_c$  is the minimum safe distance required for changing lane.  $D_s$  is the reserved distance between the ego-vehicle and the obstacle vehicle behind it after a successful lane change.  $v_c$  is the speed before the lane change,  $\bar{v}$  is the average speed during the lane change process.  $v_{max}^*$  is the maximum speed required for changing lane, and  $v_{lim}$  is the limit speed for lane changing.  $D_s$ ,  $D_c$ ,  $\bar{v}$  and  $v_{lim}$  are respectively represented as Eq.(39).

Where,  $L_T$  is the length of the vehicle,  $T$  is the delay time of braking, and  $L$  is the minimum width that needs to be met when changing lanes horizontally.

$$\begin{cases} D_s = L_T + v(t)T + \frac{v(t)^2}{2a_{max}} \\ D_c = 2 \frac{v_c - v_{obs}}{v_c} \sqrt{R^2 - \left(R - \frac{L}{2}\right)^2} \\ \bar{v} \geq (D + L_T + D_s) / 10 + v_{ego} \\ v_{max}^* = 2 \cdot \bar{v} - v_c \\ v_{lim} = \min \left( v_{max}, v_c + \int_0^{t_a} a(t) dt \right) \end{cases} \quad (39)$$

When the ego-vehicle exceeds the obstacle vehicle by 5m, the ego-vehicle begins to slow down and return to the lane it was in before changing lanes, marking the end of the entire lane changing process. Assuming the lane change time is  $t_a$ , the speed of this process is defined as Eq.(40).

$$v(t) = v_c + \int_0^{t_a} a(t) dt \quad (40)$$

In the Eq.(40),  $v_c$  is the speed before changing lane.

#### (4) Lateral meeting condition

The predicted collision region is set as a rectangular area with the width of the vehicle as the side length. The time when

the head of the ego-vehicle first reaches the collision region from the current moment is  $t_{ego-f}$ , and the time when the tail of the ego-vehicle leaves the collision domain is  $t_{ego-r}$ .

The time for the head of the obstacle vehicle to reach the collision region for the first time from the current moment is  $t_{obs-f}$ , and the time for the tail of the vehicle to leave the collision region is  $t_{obs-r}$ . The driving aggressiveness of the ego-vehicle and the obstacle vehicle is set to  $s_{ego}$  and  $s_{obs}$  respectively, which can be obtained by the vehicle networking system. According to the driving state parameters of the ego-vehicle and the obstacle vehicle, the speed planning of lateral meeting condition is designed, as shown in Figure 18.

Taking accelerating as an example, the target speed  $v_g$  should be solved. The time for the obstacle vehicle to reach the collision area is  $t$ . The time for the ego-vehicle to reach the collision area must be less than  $t$ . The distance detected by the sensor from the ego-vehicle to the collision area is  $X$ . So the average speed  $\bar{v}$  of the ego-vehicle accelerating through the collision area is  $(X + D_s) / t$ , where  $D_s$  is the safe distance. The acceleration  $a$  is given, then  $v_g$  can be calculated based on  $\bar{v}$  and  $t$ .

#### (5) Emergency obstacle avoidance

The speed planning function for vehicle emergency obstacle avoidance is:  $v_t = v_{ego} + a_{min}t$ . Where,  $v_{ego}$  is the vehicle speed before emergency braking,  $a_{min}$  is the braking deceleration, which depends on the motion state of the ego-vehicle and obstacle, and is also limited by the power system of the vehicle.

## V. SIMULATION AND EXPERIMENT OF THE TRAJECTORY PLANNING ALGORITHM

### A. TRAJECTORY PLANNING ALGORITHM BASED ON IMPROVED APF AND VEHICLE DYNAMICS CONSTRAINT

In order to avoid large changes in planning path, real-time constraints and boundary constraints are proposed as follows:

$$\begin{cases} |v_{n+1} - v_n| \leq \max \Delta v \\ |\theta_{n+1} - \theta_n| \leq \max \Delta \theta \\ |a_{n+1} - a_n| \leq \max \Delta a \\ (x, y, v, a, \theta)_{t=0} = (x_0, y_0, 0, 0, \theta_0) \\ (x, y, v, a, \theta)_{t=t_f} = (x_g, y_g, 0, 0, \theta_g) \end{cases} \quad (41)$$

where,  $\max(\Delta v)$  is the maximum increase in the vehicle speed during time step  $\Delta t$ ,  $\max(\Delta \theta)$  is the maximum increase in the vehicle heading angle during time step  $\Delta t$ , and  $\max(\Delta a)$  is the maximum increase in the vehicle acceleration during time step  $\Delta t$ .

The trajectory planning algorithm based on the improved APF and vehicle dynamics constraints.

Firstly, the obstacles in the driving environment are screened, and a high-precision driving risk field model is established based on this. Secondly, based on the decision-making process under the proposed overtaking condition and lateral meeting condition, the priority of obstacle avoidance decision-making is defined. The velocity and acceleration constraints are established based on the motion

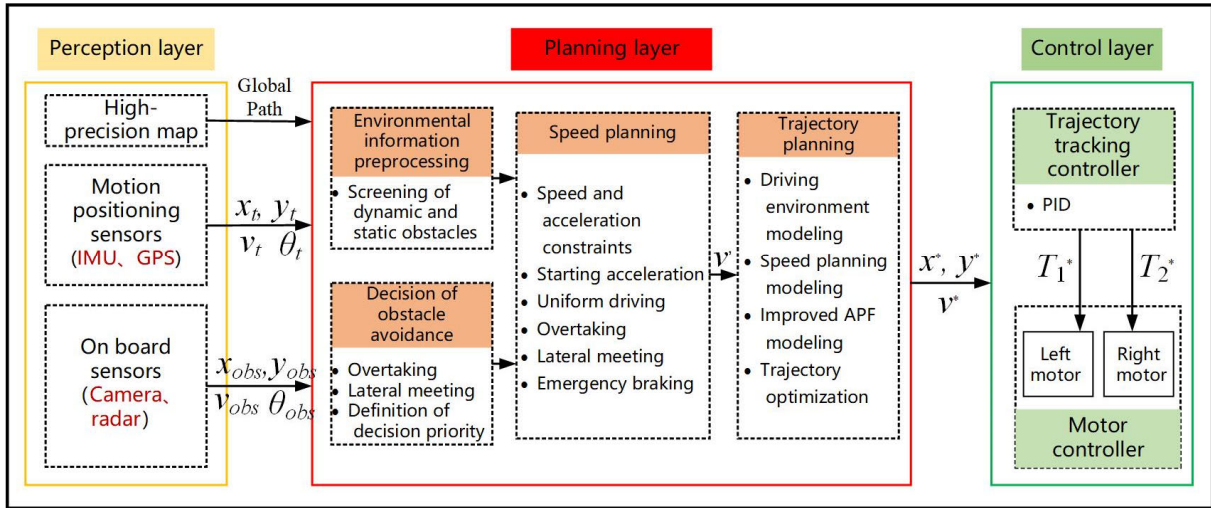


FIGURE 19. Framework of trajectory planning algorithm based on improved APF.

characteristics of the tracked vehicle, and the speed planning strategy is proposed according to the behavior decision and obstacle avoidance conditions. Finally, based on the proposed improved APF and the speed planning algorithm, a trajectory planning strategy is proposed, and planned trajectory is optimized and improved by Bézier curve. The proposed trajectory planning algorithm framework is shown in Figure 19.

1) ESTABLISHMENT OF A CO-SIMULATION PLATFORM

The driving environment and the obstacle vehicle model are built in the software Prescan, the proposed trajectory planning and a tracking controller are built in Matlab / Simulink, and a dynamic model of the tracked vehicle driven by dual motors is built in the software Adams. Finally, the co-simulation platform is built as shown in Figure 20.

B. SIMULATION RESULTS

1) OVERTAKING CONDITION UNDER STATIC OBSTACLES

As shown in Figure 21, there are three static obstacle vehicles ahead of the ego-vehicle, with the lateral distance of 2.5m between adjacent obstacle vehicles. The initial speed of the ego-vehicle  $v_0$  is 0, and target speed  $v_t$  is 18km/h. The simulation results are shown in Figure 22.

From Figure 22, it can be seen that the trajectory, the heading angle, the lateral displacement and the distance to obstacle are all very close to the expected values, which proves the effectiveness of the proposed algorithm.

2) OVERTAKING CONDITION UNDER DYNAMIC OBSTACLE

Simulation of the trajectory planning for the lane changing overtaking and obstacle avoidance condition is conducted. As shown in Figure 23, the speed of the ahead dynamic obstacle vehicle  $v_{obs}$  is 7.2km/h. The initial speed of the ego-vehicle  $v_t$  is 0, and the target speed is 18km/h. The simulation results are shown in Figure 24.

According to Figure 24, when the improved APF is used to plan trajectory for the overtaking lane change, the trajectory

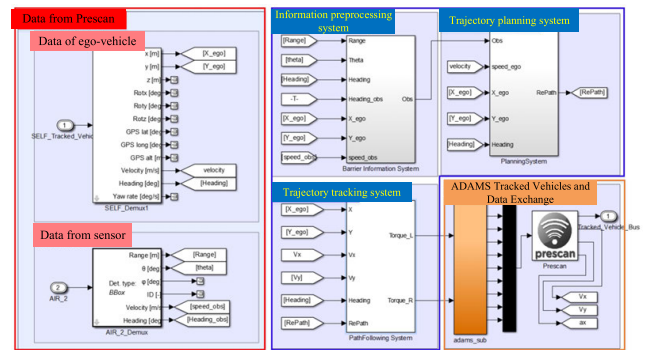


FIGURE 20. Co-simulation platform for Prescan-Adams-Matlab/Simulink.

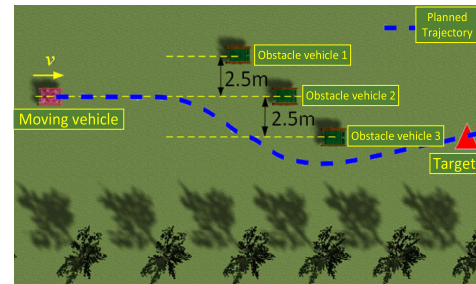


FIGURE 21. Obstacle avoidance scene of multiple static obstacles.

is smoother. The heading angle decreases from 0.35rad to 0.2rad and decreased by 42.9%. The lateral displacement decreases from 4.3m to 2.6m decreased by 39.5%.

3) DECELERATED AVOIDANCE UNDER LATERAL MEETING CONDITION

When a dynamic vehicle comes from the side, the ego-vehicle needs to accelerate or decelerate to avoid collision, trajectory planning for obstacle avoidance in this scenario is challenging.

As shown in Figure 25,  $v_{obs} = 14.4\text{km/h}$ ,  $v_t = 18\text{km/h}$ . In order to avoid collision at intersections, the ego-vehicle decelerates to avoid the driving obstacle vehicle. Form

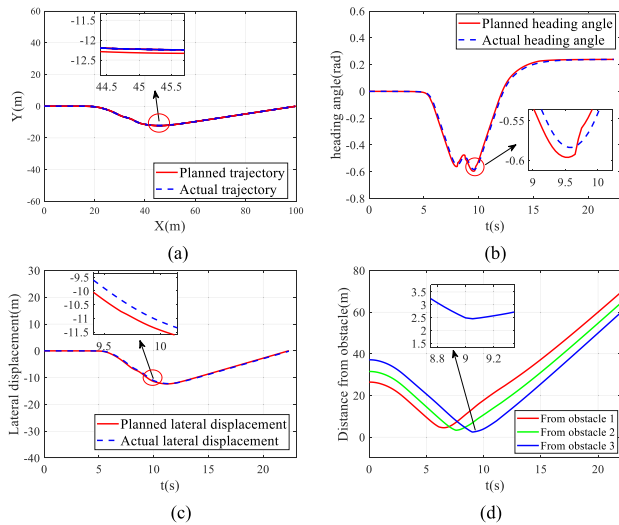


**FIGURE 22.** Simulation results of obstacle avoidance for multiple static obstacles (a) Trajectory, (b) Heading angle, (c) Lateral displacement, (d) Distance from obstacle.

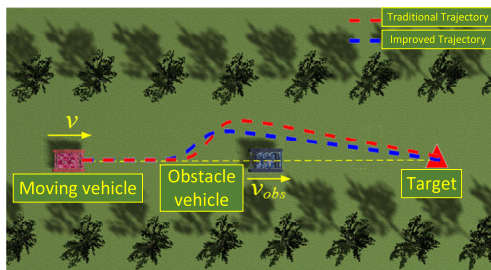


**FIGURE 23.** Obstacle avoidance scene of overtaking.

Figure 25, due to not considering speed planning, the ego vehicle collides with the driving obstacle vehicle. The simulation results of the speed and the distance from obstacle without speed planning algorithm is shown in Figure 26.

From Figure 26 (a), it can be seen that although the speed of ego-vehicles has changed, the amount of change is not significant, indicating that the ego-vehicle has not slowed down sufficiently to avoid obstacles. As shown in Figure 26 (b), the minimum distance between the ego-vehicle and the obstacle is 0, indicating a collision between the two.

After adding the speed planning algorithm, the ego-vehicle does not collide with the obstacle vehicle in Figure 27. From Figure 28(a), the ego-vehicle slows down from 17km/h to 9km/h for a period of time after detecting an obstacle. the obstacle vehicle has passed, the ego-vehicle begins to accelerate to the target speed until it reaches the target point. In Figure 28(b), the minimum distance between the ego-vehicle and the obstacle vehicle is 5.6m, and there is no risk of collision.

#### 4) ACCELERATED AVOIDANCE UNDER LATERAL MEETING CONDITION

As shown in Figure 29,  $v_{obs}=10.8km/h$ ,  $v_t=18km/h$ , the obstacle vehicle and the ego-vehicle meet at the intersection, and the simulation results are shown in Figure 30.

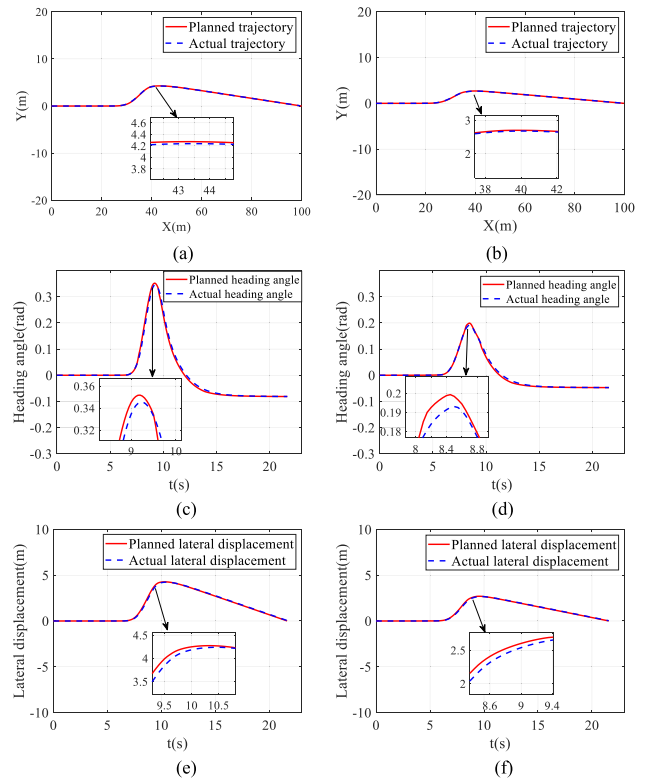


**FIGURE 24.** Comparison of the simulation results for the obstacle avoidance based on traditional APF and improved APF (a) Traditional trajectory, (b) Improved trajectory, (c) Traditional heading angle, (d) Improved heading angle, (e) Traditional lateral displacement, (f) Improved lateral displacement.

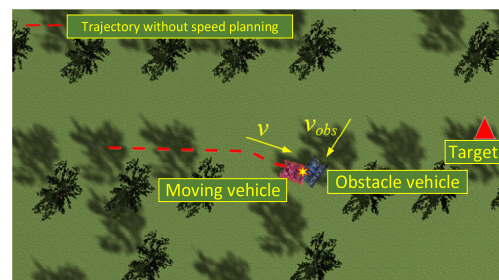


**FIGURE 25.** Deceleration and dynamic obstacle avoidance of ego-vehicle without speed planning algorithm.

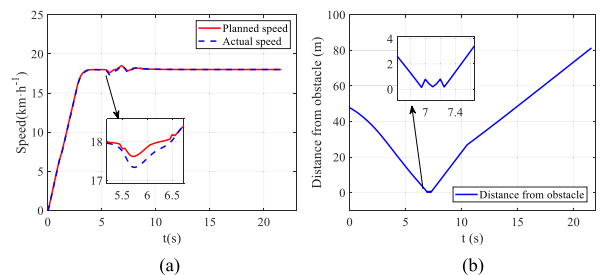


**FIGURE 26.** Simulation Results of obstacle avoidance trajectory planning without speed planning algorithm (a) Speed, (b) Distance from obstacle.

As shown in Figure 30(c)and(d), the curvature of the vehicle trajectory reduces by 70%. From Figure 30(e)~(f), it can be seen that the minimum distance between the vehicle and the obstacle vehicle with speed planning is 2.5m, which is about 1m larger than the distance without speed planning.

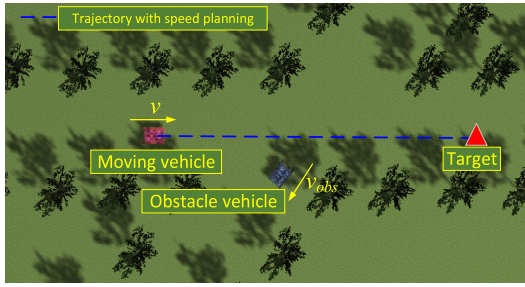


FIGURE 27. Deceleration and dynamic obstacle avoidance of ego-vehicle with speed planning algorithm.

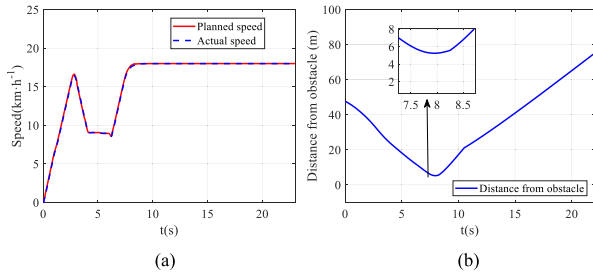


FIGURE 28. Simulation Results of obstacle avoidance trajectory planning (a) Speed, (b) Distance from obstacle with speed planning algorithm.

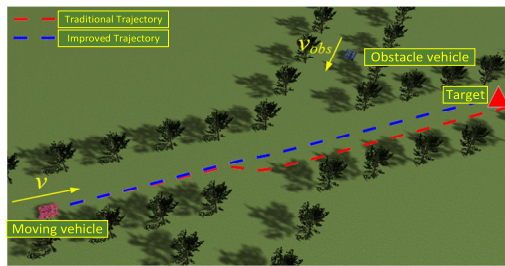


FIGURE 29. Obstacle avoidance scene of lateral dynamic obstacle.

From Figure 30(g)~(l), it can be seen that the change in vehicle heading angle with speed planning reduces by 84%, and the lateral displacement reduces by 1.25m.

In summary, the proposed trajectory planning with speed planning results in smoother and shorter trajectories, and almost no lateral displacement. Therefore, the vehicle does not make significant turns, ensuring safety while improving driving efficiency.

### C. HARDWARE-IN-LOOP EXPERIMENT

Based on dSPACE, a hardware-in-the-loop simulation experiment platform is built, as shown in Figure 31.

As shown in Figure 32, a more complex multi obstacles environment that may appear in future wars is established, including seven dynamic obstacles and one static obstacle. Dynamic obstacles are approaching ego-vehicle from different directions. The ego-vehicle needs to avoid these unknown obstacles in real-time before moving to the target point.

Assuming the target speed of the ego-vehicle is 18km/h, and the target point is located 125 meters ahead of the ego-vehicle. Those obstacle vehicles and the ego-vehicle start simultaneously. The simulation results of trajectory planning based on traditional APF are shown in Figure 33.

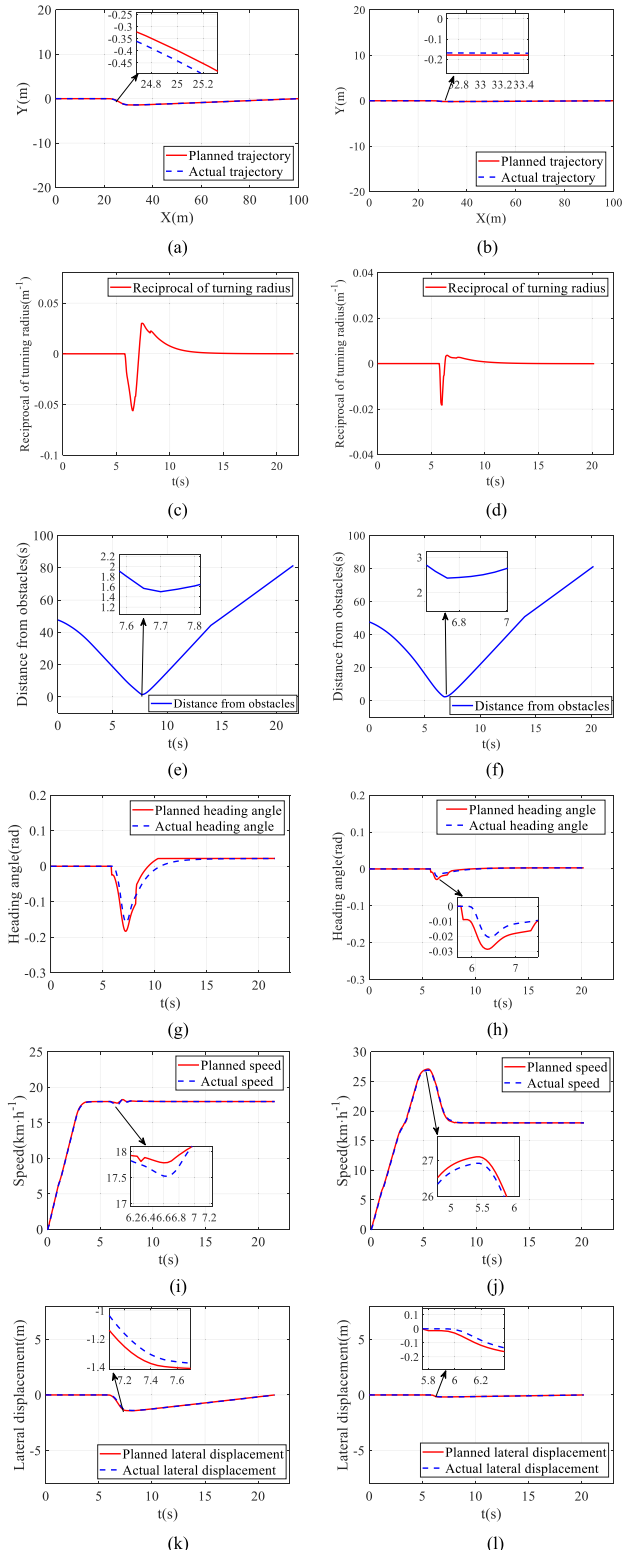


FIGURE 30. Comparison of simulation results for obstacle avoidance trajectory planning with and without speed planning (a) Trajectory without speed planning, (b) Trajectory with speed planning, (c) Radius without speed planning, (d) Radius with speed planning, (e) Distance without speed planning, (f) Distance with speed planning, (g) Heading angle without speed planning, (h) Heading angle with speed planning, (i) Speed without speed planning, (j) Speed with speed planning, (k) Lateral displacement without speed planning, (l) Lateral displacement with speed planning.

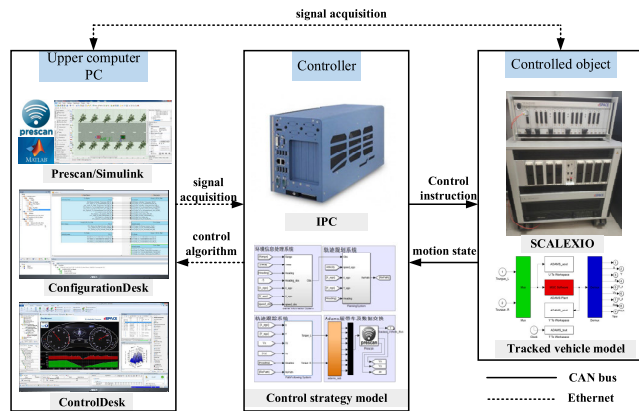


FIGURE 31. HIL simulation platform based on dSPACE.

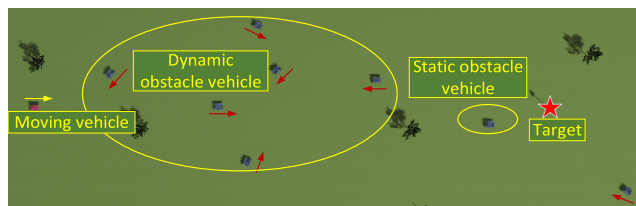


FIGURE 32. Obstacle avoidance scene of complex dynamic obstacles.

From Figure 33(a)~(b), it can be seen that the planned path for obstacle avoidance based on traditional APF has more turns and longer distance. Additionally, there is almost no change in vehicle speed throughout the entire process, which is not in line with actual driving habits. From Figure 33(c)~(d), it can be seen that the turning radius and the heading angle undergo at least 6 significant changes over time. Among them, the maximum change in heading angle is 0.72 rad. According to Figure 33(e), the maximum lateral displacement reaches 5.6m. As shown in Figure 33(f), the dotted lines of different colors are the distance from the ego-vehicle to the different obstacles, and the red solid line is the shortest distance envelope. There is a zero distance between the ego-vehicle and two obstacles, and the minimum distance from an obstacle is less than 1m, indicating that a collision accident has occurred. Therefore, the planning algorithm based on the traditional APF cannot guarantee the safe obstacle avoidance of the vehicle in scene with dynamic obstacles. The improved APF and speed planning are used to plan the trajectory of the same scene. The results are shown in Figure 34.

Compared with the results Figure 33(a), the trajectory planning based on the improved APF in Figure 34(a) takes into account speed planning, resulting in fewer turns and shorter path. From Figure 34(b), it can be seen that the vehicle undergoes four stages of acceleration-deceleration-acceleration-deceleration during driving, and finally returns to the target speed, indicating that the corresponding speed planning strategy is used when the ego-vehicle encounters different obstacles. Compared with the results in Figure 33(c)~(d), in Figure 34(c)~(d), The maximum amplitude of change

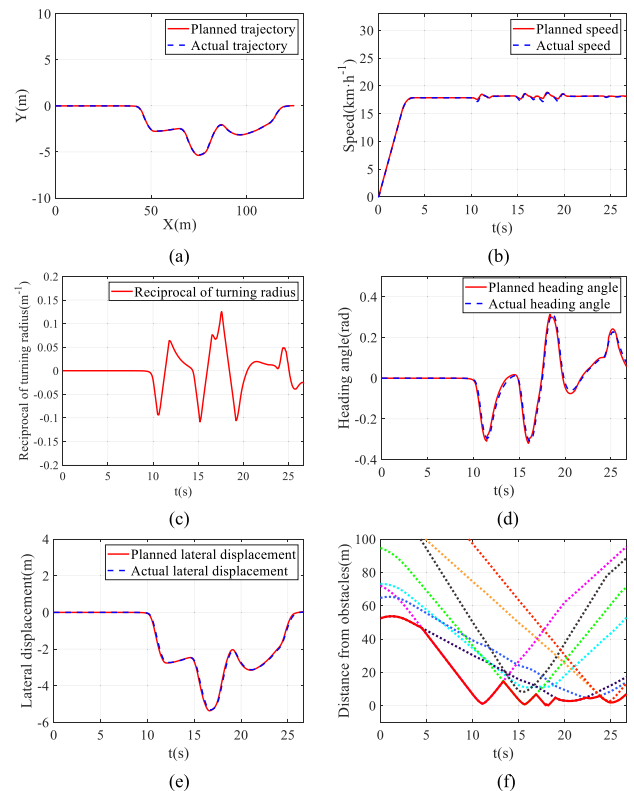
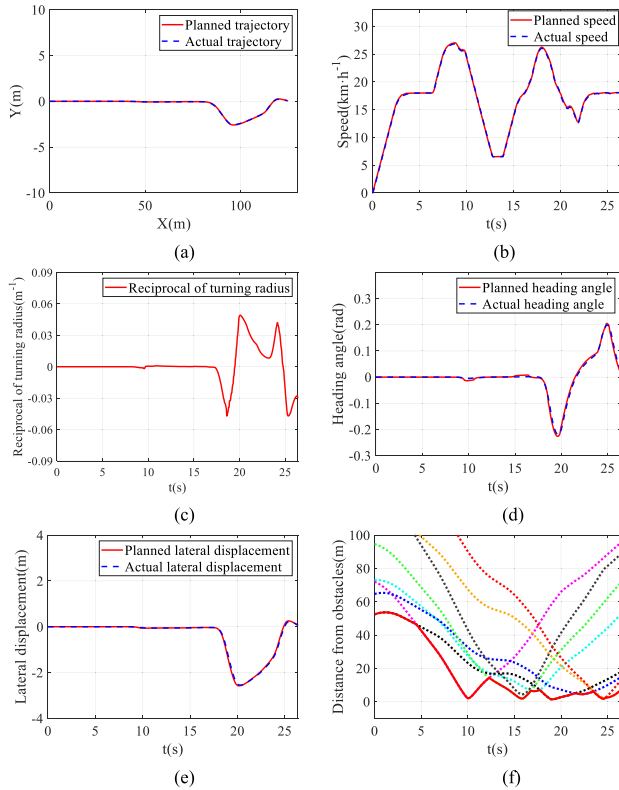


FIGURE 33. Simulation results of trajectory planning based on the traditional APF (a) Trajectory, (b) Speed, (c) Turning radius, (d) Heading angle, (e) Lateral displacement, (f) Distance from obstacles.

in the turning radius of the ego-vehicle has decreased from 44.15m to 16.26m, resulting in a decrease of 63.2%, and the maximum amplitude of change in the ego-vehicle's heading angle has decreased from 0.64rad to 0.4rad, resulting in a decrease of 37.5%. This proves that the trajectory obtained by using the improved trajectory planning method is smoother and more efficient. In Figure 34(e), the maximum lateral displacement is 2.5m and reduced by 3.1m than that in traditional APF method. From Figure 34(f), it can be seen that the minimum distance between the ego-vehicle and the obstacle vehicle is 1.524m, and there is no collision. Therefore, the planned trajectory is safe and reliable.

#### D. EXPERIMENT RESULTS

To further verify the control effectiveness and real-time performance of the proposed trajectory planning strategy based on the improved APF on a real vehicle. A dual motor driven tracked unmanned platform is constructed as shown in Figure 35. The proposed improved APF trajectory planning strategy is run on an industrial computer ROS system. Experiments on obstacle avoidance trajectory planning for static obstacles are conducted to verify the effectiveness of the proposed method. From the experimental results in Figure 36, it can be seen that the planned trajectory is smooth and safe, and the tracked vehicle can track the planned trajectory in real-time with small deviations.



**FIGURE 34.** Simulation results of trajectory planning based on improved APF (a) Trajectory, (b) Speed, (c) Turning radius, (d) Heading angle, (e) Lateral displacement, (f) Distance from obstacles.

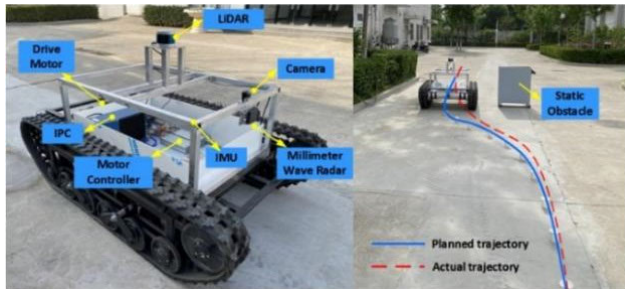


**FIGURE 35.** Experimental vehicle and the experimental scenario.

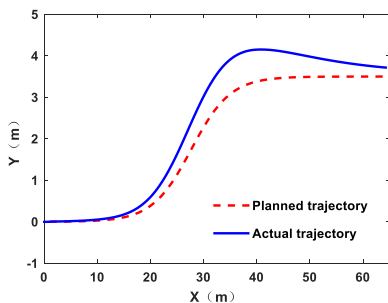


**FIGURE 36.** Experimental results: the trajectory.

**VI. CONCLUSION**

A trajectory planning algorithm based on improved APF integrating speed planning was proposed in this paper, improving the efficiency and safety of trajectory planning for tracked vehicles.

(1) After the APF method is improved, the lane changing track is smoother, and the change of track curvature is smaller. The change of heading angle is reduced by 42.9%, the lateral displacement between the ego-vehicle and the obstacle vehicle is reduced by 39.5%, improving the driving efficiency of the vehicle.

(2) The trajectory planning algorithm that integrates speed planning is proposed in this paper. When encountering lateral dynamic obstacles, the vehicle will carry out speed planning in advance to avoid obstacles. The experimental results show that the number of drastic changes in turning radius and heading angle of the vehicle is significantly reduced, and the maximum amplitude was reduced by 63.2% and 37.5% respectively, making the vehicle’s obstacle avoidance and lane changing safer, smoother, and more efficient.

**REFERENCES**

- [1] P. Zhang, C. Zhang, and W. Gai, “Research on system analysis and development issues of the unmanned combat platform,” in *Proc. 2nd Int. Symp. Comput. Eng. Intell. Commun. (ISCEIC)*, Nanjing, China, Aug. 2021, pp. 372–376, doi: 10.1109/ISCEIC53685.2021.00084.
- [2] T. Mercy, R. Van Parys, and G. Pipeleers, “Spline-based motion planning for autonomous guided vehicles in a dynamic environment,” *IEEE Trans. Control Syst. Technol.*, vol. 26, no. 6, pp. 2182–2189, Nov. 2018.
- [3] D. González, J. Pérez, R. Lattarulo, V. Milanés, and F. Nashashibi, “Continuous curvature planning with obstacle avoidance capabilities in urban scenarios,” in *Proc. 17th Int. IEEE Conf. Intell. Transp. Syst. (ITSC)*, Oct. 2014, pp. 1430–1435.
- [4] T. Berglund, A. Brodnik, H. Jonsson, M. Staffanson, and I. Soderkvist, “Planning smooth and obstacle-avoiding B-spline paths for autonomous mining vehicles,” *IEEE Trans. Autom. Sci. Eng.*, vol. 7, no. 1, pp. 167–172, Jan. 2010.
- [5] Z. Wu, L. Sun, W. Zhan, C. Yang, and M. Tomizuka, “Efficient sampling-based maximum entropy inverse reinforcement learning with application to autonomous driving,” *IEEE Robot. Autom. Lett.*, vol. 5, no. 4, pp. 5355–5362, Oct. 2020.
- [6] L. Ma, J. Xue, K. Kawabata, J. Zhu, C. Ma, and N. Zheng, “Efficient sampling-based motion planning for on-road autonomous driving,” *IEEE Trans. Intell. Transp. Syst.*, vol. 16, no. 4, pp. 1961–1976, Aug. 2015.
- [7] R. Kala and K. Warwick, “Multi-level planning for semi-autonomous vehicles in traffic scenarios based on separation maximization,” *J. Intell. Robot. Syst.*, vol. 72, nos. 3–4, pp. 559–590, Dec. 2013.
- [8] B. V. Gurenko and M. A. Vasileva, “Intelligent system of mooring planning, based on deep Q-learning,” in *Proc. Int. Conf. Ind., Eng. Other Appl. Appl. Intell. Syst.*, Springer, Cham, 2021, pp. 369–378.
- [9] F. Eiras, M. Hawasly, S. V. Albrecht, and S. Ramamoorthy, “A two-stage optimization-based motion planner for safe urban driving,” *IEEE Trans. Robot.*, vol. 38, no. 2, pp. 822–834, Apr. 2022.
- [10] H. Guo, C. Shen, H. Zhang, H. Chen, and R. Jia, “Simultaneous trajectory planning and tracking using an MPC method for cyber-physical systems: A case study of obstacle avoidance for an intelligent vehicle,” *IEEE Trans. Ind. Informat.*, vol. 14, no. 9, pp. 4273–4283, Sep. 2018.
- [11] J. Tang, X. Chen, X. Zhu, and F. Zhu, “Dynamic reallocation model of multiple unmanned aerial vehicle tasks in emergent adjustment scenarios,” *IEEE Trans. Aerosp. Electron. Syst.*, vol. 59, no. 2, pp. 1139–1155, Apr. 2023.
- [12] J. Tang, G. Liu, and Q. Pan, “A review on representative swarm intelligence algorithms for solving optimization problems: Applications and trends,” *IEEE/CAA J. Autom. Sinica*, vol. 8, no. 10, pp. 1627–1643, Oct. 2021.
- [13] S. Aradi, “Survey of deep reinforcement learning for motion planning of autonomous vehicles,” *IEEE Trans. Intell. Transp. Syst.*, vol. 23, no. 2, pp. 740–759, Feb. 2022.
- [14] L. Zhao, E. Zhang, S. Wan, A. Hawbani, A. Y. Al-Dubai, G. Min, and A. Y. Zomaya, “MESON: A mobility-aware dependent task offloading scheme for urban vehicular edge computing,” *IEEE Trans. Mobile Comput.*, early access, Jun. 23, 2023, doi: 10.1109/TMC.2023.3289611.

- [15] X. Deng, L. Wang, J. Gui, P. Jiang, X. Chen, F. Zeng, and S. Wan, "A review of 6G autonomous intelligent transportation systems: Mechanisms, applications and challenges," *J. Syst. Archit.*, vol. 142, Sep. 2023, Art. no. 102929.
- [16] O. Khatib, "Real-time obstacle avoidance for manipulators and mobile robots," *Int. J. Robot. Res.*, vol. 5, no. 1, pp. 90–98, Mar. 1986.
- [17] D. Gregory and J. Michael, *Computational Principles of Mobile Robotics*. Cambridge, U.K.: Cambridge Univ. Press, 2000.
- [18] D. Zhang and F. Liu, "Research and prospect of path planning method based on artificial potential field method," *Comput. Eng. Sci.*, vol. 35, no. 6, pp. 88–95, 2013.
- [19] C. Thiemann, M. Treiber, and A. Kesting, "Estimating acceleration and lane-changing dynamics from next generation simulation trajectory data," *Transp. Res. Rec., J. Transp. Res. Board*, vol. 2088, no. 1, pp. 90–101, Jan. 2008.
- [20] J. Zhang, Y. He, Y. Peng, and G. Li, "Neural network and artificial potential field based cooperative and adversarial path planning," *Acta Aeronauticae Astronautica Sinica*, vol. 40, no. 3, 2019, Art. no. 322493.
- [21] A. Azzabi and K. Nouri, "An advanced potential field method proposed for mobile robot path planning," *Trans. Inst. Meas. Control*, vol. 41, no. 11, pp. 3132–3144, Jul. 2019.
- [22] M. Zhao, "Path planning method for multiple mobile robots based on modified potential field method," *Appl. Res. Comput.*, vol. 37, pp. 66–72, Dec. 2020.
- [23] G. Chen, "Research on path planning of improved artificial potential field method in unknown environments," *J. Mech. Electron.*, vol. 39, no. 5, pp. 74–80, 2021.
- [24] H. H. Triharminto, O. Wahyungoro, T. B. Adji, A. I. Cahyadi, and I. Ardiyanto, "A novel of repulsive function on artificial potential field for robot path planning," *Int. J. Electr. Comput. Eng. (IJECE)*, vol. 6, no. 6, p. 3262, Dec. 2016.
- [25] Z. Pan, C. Zhang, Y. Xia, H. Xiong, and X. Shao, "An improved artificial potential field method for path planning and formation control of the multi-UAV systems," *IEEE Trans. Circuits Syst. II, Exp. Briefs*, vol. 69, no. 3, pp. 1129–1133, Mar. 2022, doi: [10.1109/TCSII.2021.3112787](https://doi.org/10.1109/TCSII.2021.3112787).
- [26] C. Yuan, S. Weng, J. Shen, L. Chen, Y. He, and T. Wang, "Research on active collision avoidance algorithm for intelligent vehicle based on improved artificial potential field model," *Int. J. Adv. Robotic Syst.*, vol. 17, no. 3, May 2020, Art. no. 172988142091123.
- [27] B. Lu, G. Li, H. Yu, H. Wang, J. Guo, D. Cao, and H. He, "Adaptive potential field-based path planning for complex autonomous driving scenarios," *IEEE Access*, vol. 8, pp. 225294–225305, 2020.
- [28] J. Luo, Z.-X. Wang, and K.-L. Pan, "Reliable path planning algorithm based on improved artificial potential field method," *IEEE Access*, vol. 10, pp. 108276–108284, 2022, doi: [10.1109/ACCESS.2022.3212741](https://doi.org/10.1109/ACCESS.2022.3212741).
- [29] Y. Du, X. Zhang, and Z. Nie, "A real-time collision avoidance strategy in dynamic airspace based on dynamic artificial potential field algorithm," *IEEE Access*, vol. 7, pp. 169469–169479, 2019, doi: [10.1109/ACCESS.2019.2953946](https://doi.org/10.1109/ACCESS.2019.2953946).
- [30] Y. Zhang, L. Huang, and Y. Zhang, "Research on intelligent vehicle dynamic obstacle avoidance based on artificial potential field method," *Logistics Sci.-Tech.*, vol. 5, pp. 87–92, Jan. 2020.
- [31] Y. Rasekhipour, A. Khajepour, S.-K. Chen, and B. Litkouhi, "A potential field-based model predictive path-planning controller for autonomous road vehicles," *IEEE Trans. Intell. Transp. Syst.*, vol. 18, no. 5, pp. 1255–1267, May 2017.
- [32] J. Hu, Y. Hu, H. Chen, and K. Liu, "Research on trajectory tracking of unmanned tracked vehicles based on model predictive control," *Acta Armamentarii*, vol. 40, no. 3, pp. 456–463, 2019.
- [33] Z. Zhao, H. Liu, and H. Chen, "Research on trajectory prediction method of distributed high speed electric drive unmanned tracked vehicle in off-road conditions," *Acta Armamentarii*, vol. 40, no. 4, pp. 680–688, 2019.
- [34] E. Kayacan, W. Saeys, H. Ramon, C. Belta, and J. M. Peschel, "Experimental validation of linear and nonlinear MPC on an articulated unmanned ground vehicle," *IEEE/ASME Trans. Mechatronics*, vol. 23, no. 5, pp. 2023–2030, Oct. 2018, doi: [10.1109/TMECH.2018.2854877](https://doi.org/10.1109/TMECH.2018.2854877).
- [35] B. Wang, "Unified motion planning method for heterogeneous tracked vehicles," *Acta Armamentarii*, vol. 43, no. 2, pp. 241–251, 2022.
- [36] L. Zhai, X. Zhang, X. Zhang, and C. Wang, "Local dynamic obstacle avoidance path planning algorithm for unmanned vehicles based on potential field method," *J. Beijing Univ. Technol.*, vol. 42, no. 7, pp. 696–705, 2022.



Her research interests include dynamics control, and motor drive system control and EMC of EVs.

**LI ZHAI** (Member, IEEE) received the Ph.D. degree in vehicle engineering from the Beijing Institute of Technology, Beijing, China, in 2004. Since 2009, she has been an Associate Professor with the National Engineering Laboratory for Electric Vehicles and the School of Mechanical Engineering, Beijing Institute of Technology. From 2013 to 2014, she was a Visiting Scholar in electrical and computer engineering with the University of Missouri-Rolla, Rolla, MO, USA.



**CHANG LIU** received the B.S. degree in automotive engineering from Jiangsu University, Zhenjiang, China, in 2021. She is currently pursuing the M.S. degree in mechanical engineering with the Beijing Institute of Technology, Beijing, China. Her research interests include vehicle system dynamics and control and vehicle path tracking control.



**XUEYING ZHANG** received the M.S. degree in mechanical engineering from the Beijing Institute of Technology, Beijing, China, in 2022. Since 2022, she has been with the China North Vehicle Research Institute. Her research interests include vehicle system dynamics and control, model predictive control for autonomous vehicle, and vehicle path tracking control.



**CHENGPING WANG** received the M.S. degree in mechanical engineering from the Beijing Institute of Technology, Beijing, China, in 2023. Since 2023, he has been with Huawei Technologies Company Ltd. His research interests include vehicle system dynamics and control and vehicle path tracking control.